Chemical Science

ROYAL SOCIETY OF CHEMISTRY

EDGE ARTICLE

View Article Online
View Journal | View Issue

Cite this: *Chem. Sci.*, 2023, **14**, 13832

All publication charges for this article have been paid for by the Royal Society of Chemistry

Received 16th August 2023
Accepted 3rd November 2023

DOI: 10.1039/d3sc04280d

rsc.li/chemical-science

Engineering TADF, mechanochromism, and second harmonic up-conversion properties in regioisomeric substitution space†

Abhijit Chatterjee,[a] Joy Chatterjee,[a] Subrahmanyam Sappati,[b] Riteeka Tanwar,[a] Madan D. Ambhore,[c] Habibul Arfin,[a] Rintu M. Umesh,[d] Mayurika Lahiri,[d] Pankaj Mandal[a] and Partha Hazra *[a]

This research article explores the distinct TADF efficiency of three donor–acceptor based regio-isomers: DPAOCN (*ortho*-isomer), DPAMCN (*meta*-isomer), and DPAPCN (*para*-isomer). DPAPCN exhibits maximum TADF efficiency in both solution and solid-state with an impressive reverse inter-system crossing (RISC) rate of $\sim 10^6$ s^{-1}; the underlying cause being the minimum singlet-triplet splitting energy or ΔE_{ST} and maximum SOC (spin–orbit coupling) between the S_1 & T_1 states. Apart from TADF, differences in crystal packing of the regio-isomers result in intriguing bulk phase properties. DPAOCN, with its non-centrosymmetric $P2_12_12_1$ space group and substantial crystal void volume, exhibits reversible tri-color mechanochromic luminescence behavior, while the *meta* and *para* isomers, due to their centrosymmetric packing and diminished crystal void volume, remain inert to mechanical pressure. Expanding the horizon of possibilities, the non-centrosymmetric nature of *ortho*-isomer further renders it an excellent SHG material, with a $\chi^{(2)}$ value of 0.19 pm V^{-1} at 1220 nm and a laser-induced damage threshold (LIDT) value of 13.27 GW cm^{-2}. Overall, a comprehensive investigation into the regio-isomers has been carried out, encompassing their TADF, SHG, and mechanochromic luminescent properties.

Introduction

Multifunctional organic luminescent materials with delayed fluorescence and phosphorescence have revolutionized the field of optoelectronics by providing a flexible platform for applications in organic light-emitting diodes (OLEDs), bio-imaging, sensing, and photocatalysis.[1–8] Over the last decade, plenty of attempts have been made towards improving TADF efficiencies, minimizing the efficiency roll-off, and expanding the scope of these prodigious emitters to be utilized in bright OLED displays. Several effective strategies have been implemented, such as enhancing intramolecular charge transfer (ICT),[9–11] increasing molecular rigidity,[12,13] incorporating through-space charge transfer (TSCT),[14,15] and so on. All these strategies involve significant structural modifications that encompass major perturbations in the molecular architecture to fine-tune TADF properties. Nevertheless, there remains a lack of generalized strategies for well-directed customization of the molecular skeleton of the emitters, which can moderately enhance the TADF efficiency while keeping all other associated properties unperturbed. It is of utmost importance to incorporate such changes through minimal structural modulation so that productivity and cost-effectiveness can be maintained. Also, it is crucial to avoid changing the functional groups or the overall molecular skeleton, as this can sometimes have a dramatic impact[16,17] and may lead to conclusions that do not correspond to the actual design strategy. In this aspect, regioisomerism may be an important step forward, as it can also affect the energy levels (both singlets and triplets) of a chromophore with minimal structural change. The introduction of regio-isomers to improve TADF functionalities is still under development and is restricted to a few structural frameworks.[18,19] Moreover, simultaneous tuning of TADF efficiencies along with color changes over a wider range remains elusive to date.

Our research hereby focuses on exploring a methodology that involves three regio-isomers (*ortho*, *meta*, and *para*) based on diphenylamine donors and dicyano benzene-based

[a]*Department of Chemistry, Indian Institute of Science Education and Research (IISER), Pune 411008, Maharashtra, India. E-mail: p.hazra@iiserpune.ac.in*

[b]*Department of Pharmaceutical Technology and Biochemistry and Bio Tech Med Center, Gdańsk University of Technology, Gdańsk 80233, Poland*

[c]*Department of Chemistry, Yeshwant Mahavidyalaya Nanded, Nanded, PIN-431602, Maharashtra, India*

[d]*Department of Biology, Indian Institute of Science Education and Research (IISER), Pune 411008, Maharashtra, India*

† Electronic supplementary information (ESI) available: Instrumentation, materials, experimental details, crystallographic data, characterization data and respective spectra, computational details (DFT) including co-ordinates, and optical properties in solid and solution states. Temperature dependent studies and applications are provided. CCDC 2271434, 2287184 and 2287185. For ESI and crystallographic data in CIF or other electronic format see DOI: https://doi.org/10.1039/d3sc04280d

acceptors (Scheme 1). These isomers provide sequential control of emission characteristics and TADF efficiencies. It is worth noting that Ishimatsu *et al.* with a similar kind of molecular scaffold demonstrated how a set of carbazole-based TADF molecules can produce intense green to red electrogenerated chemiluminescence (ECL).[20] They also explained the solvent polarity effect on the RISC kinetics of a popular TADF molecule, 4CzIPN.[21] Our study takes a different approach, focusing on cost-effective structural changes that can efficiently tune the singlet-triplet energy gap and improve thermal up-conversion efficiency. The results in solution, doped film, and powdered states show an increasing rate of reverse-intersystem crossing (RISC) from *ortho* to *para* isomers which is consistent with experimentally calculated ΔE_{ST} values along with a wide range of emission color tunability from green to red. The RISC rates can even go up to $\sim 10^6$ s^{-1} in the *para*-isomer compared to $\sim 10^2$–10^4 s^{-1} of the *ortho*-isomer. The electroluminescence potential of all three isomers has been further explored through the fabrication of converted LEDs (c-LEDs) with three different emission colors. Moreover, these three different regio-isomers inherently induce perturbations in the symmetry elements at the molecular level, which modulates the crystal packing arrangement and induces anisotropy in the polarizability of the condensed bulk phase and results in the revelation of important bulk properties such as mechanochromic luminescence (MCL), non-linear optical (NLO) properties such as second harmonic generation (SHG), and so on.[22–24] The insertion of molecular asymmetry in the *ortho*-isomer led to a non-centrosymmetric $P2_12_12_1$ crystal space group, resulting in excellent reversible tri-color mechanochromic luminescence characteristics and making it a superb SHG material with a $\chi^{(2)}$ value of 0.19 pm V^{-1} at 1220 nm and laser-induced damage threshold (LIDT) value of 13.27 GW cm^{-2}. Furthermore, due to the charge transfer nature of all three isomers, they are active for two-photon absorption, which has been further exploited for two-photon excited confocal cell imaging without compromising cellular viability.

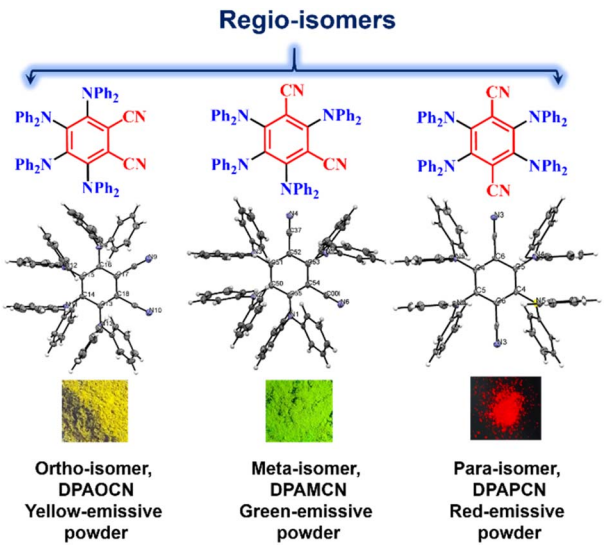

Scheme 1 Molecular structures of all three regio-isomers.

Altogether, this work explores the multi-faceted nature of three donor–acceptor regioisomers with a major focus on TADF, SHG, and mechanochromic luminescent properties. Based on molecular level understanding and bulk phase properties, the *para*-isomer is identified as the most efficient TADF emitter with the largest RISC rate, whereas the *ortho*-isomer is judiciously extracted as the one to manifest simultaneous TADF, mechanochromic luminescence, and SHG properties.

Results and discussion

Charge-transfer emission and TADF properties

All the compounds show two successive broad absorption bands in toluene. The bands were named high energy (HE) bands and low energy (LE) bands. The HE bands are located within 320–420 nm, 310–430 nm, and 320–400 nm for DPAOCN, DPAMCN, and DPAPCN, respectively. The LE bands are located in the range of 430–490 nm, 440–500 nm, and 440–550 nm for DPAOCN, DPAMCN, and DPAPCN, respectively (Fig. 1). The emergence of the HE band can be attributed to the molecular π–π* transition and the LE band to the charge transfer (CT) transition from the peripheral diphenyl donor moieties to the core acceptor moiety. Well-separated HOMOs and LUMOs obtained from density functional theory (DFT) calculations at the CAM-B3LYP/6-311++G (d,p) level (Fig. S1†) and polarity-

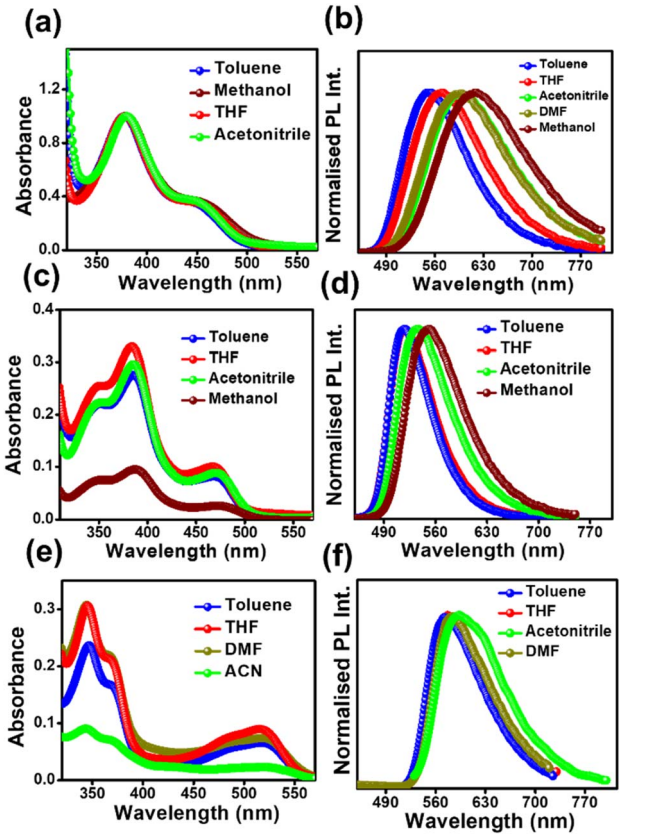

Fig. 1 Absorption and emission spectra of (a) & (b) DPAOCN, (c) & (d) DPAMCN, and (e) & (f) DPAPCN in solvents of different polarities (10 μM concentration).

dependent emission spectra (Fig. 1) further confirm our conjecture about the charge transfer natures of our probes. Notably, the extent of red shift in the emission maxima is most pronounced in DPAOCN, which exhibits a substantial ~45 nm red shift while altering the solvent from toluene to acetonitrile. On the other hand, DPAMCN and DPAPCN display a smaller redshift of 22 nm and 20 nm, respectively, suggesting the highest dipole moment of DPAOCN in the excited state. The computed dipole moments obtained from the optimized S_1 state geometries (Fig. S3†) confirm the trend further, with the largest S_1 state dipole moment in DPAOCN (7.88 D), followed by DPAMCN (5.90 D) and the least in DPAPCN (0.002 D). Furthermore, the investigation of emission lifetime across varying solvent polarities provides a comprehensive elucidation of the excited states. In DPAOCN, the lifetime of the mono-exponential decay profile increases from 3.57 ns to 5.35 ns when the solvent is changed from toluene to THF. However, the lifetime decreases to 1.25 ns in a highly polar solvent such as methanol, indicating a total charge separation and increased non-radiative decay in highly polar solvents (Fig. S4 and Table S1†). In contrast, DPAMCN and DPAPCN, owing to their lower excited state dipole moments, lead to an incomplete charge separation process (Fig. S4 and Tables S2 and S3†). As a result, the fluorescence lifetime shift in variable solvent polarity is less pronounced than that observed in DPAOCN. Next, the fluorescence up-conversion technique was employed to investigate the ultra-fast dynamical processes in excited states. In the case of DPAOCN in toluene, the decay kinetics (excitation 400 nm and collection wavelength 530 nm) exhibits a bi-exponential behavior, with a short decay component of approximately 6 ps, having a contribution of 37% ± 0.8% along with a very long radiative decay (with a lifetime of ~3.5 ns). Interestingly, when the collection wavelength is progressively increased to 550 nm and subsequently to 560 nm, the contribution of the 6 ps decay transient decreases to 7% ± 1.14% (at 550 nm) and becomes negligible at 560 nm (Fig. S5 and Table S4†). Similar observations are obtained for DPAMCN and DPAPCN, however, with different magnitudes of short and long decay components (Fig. S5 and Table S4†). The rapid decay component in all three isomers can be attributed to the conformational relaxation process following photoexcitation and subsequent formation of the charge transfer state.

In order to confirm the TADF process, photo-physical studies were carried out in degassed toluene. All three luminogens in degassed toluene experience an enhanced PL intensity compared to their aerated form (Fig. 2a–c). Furthermore, the time-gated emission spectra in degassed toluene completely overlapped with the steady-state emission spectra for all three isomers, indicating the occurrence of TADF (Fig. 2d–f). Fractional quantum yields of both prompt and delayed fluorescence (Φ_{PF} & Φ_{DF}), measured from the toluene degassing experiment dictate the highest delayed fluorescence contribution in the *para*-isomer (Fig. 2a–c & Table 1). Additionally, the delayed fluorescence lifetimes in degassed toluene were found to be longest in the *ortho*-isomer and shortest in the *para*-isomer (1.01 ms for DPAOCN, 695 μs for DPAMCN, and 4.13 μs for DPAPCN) (Fig. S6†). From the onset of TADF and

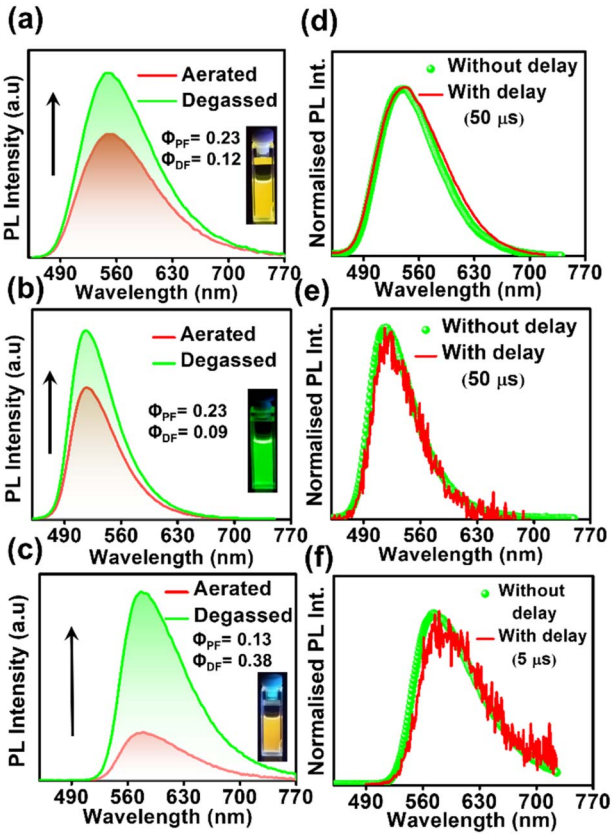

Fig. 2 Emission spectra in aerated and degassed toluene of (a) DPAOCN, (b) DPAMCN, and (c) DPAPCN (for 30 μm of luminogen concentration). Steady-state and time-gated emission spectra in degassed toluene of (d) DPAOCN, (e) DPAMCN, and (f) DPAPCN. 2 ms sample windows were used for DPAOCN and DPAMCN, whereas for DPAPCN, a 1 ms sample window was used for gated spectra measurement.

phosphorescence emission bands (Fig. S7†), the calculated ΔE_{ST} values are found to be highest in DPAOCN (0.27 eV) and lowest in DPAPCN (0.05 eV) (Table 1). From the calculated reverse inter-system crossing (RISC) rates, the maximum k_{RISC} rate is found in the case of DPAPCN ($\sim 10^6$ s^{-1}), while the rate is minimum in DPAOCN ($\sim 10^2$ s^{-1}) (Table 1), which is in accordance with the energy barrier law. The variation of ΔE_{ST} in all three regio-isomers is consistent with the trends obtained from the TDDFT calculations *i.e.* the maximum in the case of DPAOCN and minimum in DPAPCN (Fig. S8†). As the rate of the reverse intersystem crossing process (k_{RISC}) is crucially dependent upon the nature of the two states involved, it is important to reveal the nature of the S_1 and T_1 states. The RISC rate is more pronounced when the S_1 state has more charge transfer (CT) character and the T_1 state carries more locally excited (LE) character or *vice versa* due to enhanced spin–orbit coupling between such states, which is in accordance with the El-Sayed rule.[25] Natural transition orbital (NTO) calculations show that, in all three cases, the hole and electron orbitals of the S_1 state are spatially well separated suggesting a predominant CT behavior of the S_1 state which is well-corroborated with the experimental results. For the T_1 state, however, all three

Table 1 Photophysical data of all three regio-isomers in different states. All the quantum yields have been measured using an integrated sphere. ϕ_{PF} and ϕ_{DF} signify fractional quantum yield of prompt fluorescence and delayed fluorescence, respectively

Compound	ϕ_{PF}	ϕ_{DF}	E_{S1} [eV]	E_{T1} [eV]	ΔE_{ST} [eV]	k_r[a] (S_1–S_0) (s^{-1})	k_{ISC}[b] (S_1–T_1) (s^{-1})	k_{RISC}[c] (T_1–S_1) (s^{-1})
DPAOCN								
Solution[d]	0.23	0.12	2.60	2.33	0.27	6.4×10^7	2.1×10^8	6.7×10^2
Film	0.21	0.43	2.46	2.29	0.17	4.7×10^7	1.8×10^8	2.0×10^4
Powder	0.02	0.22	2.46	2.24	0.22	9.1×10^6	4.5×10^8	3.0×10^4
DPAMCN								
Solution[d]	0.23	0.09	2.58	2.38	0.20	1.3×10^8	4.5×10^8	7.3×10^2
Film	0.04	0.65	2.45	2.35	0.10	3.2×10^7	8.0×10^8	1.6×10^5
Powder	0.02	0.12	2.47	2.26	0.21	1.8×10^7	9.0×10^8	1.8×10^5
DPAdPCN								
Solution[d]	0.13	0.38	2.32	2.27	0.05	7.5×10^7	5.0×10^8	8.1×10^5
Film	0.03	0.93	2.25	2.19	0.06	1.6×10^7	5.4×10^8	2.9×10^6
Powder	0.02	0.26	2.14	2.05	0.09	2.4×10^7	1.2×10^9	7.8×10^6

[a] k_r (S_1–S_0) = ϕ_{PF}/τ_{PF}. [b] k_{ISC} ($S_1 - T_1$) = $(1 - \phi_{PF})/\tau_{PF}$. [c] k_{RISC} (T_1–S_1) = $\phi_{DF}/(k_{ISC}\tau_{PF}\,\tau_{DF}\phi_{PF})$. [d] Measured using 30 μm of sample concentration under aerated and degassed conditions.

molecules exhibit a predominant locally excited (LE) nature due to spatially superimposed hole and electron pairs in both significant NTO pairs (Fig. 3). This is also supported by our experimental findings where the T_1 state emission at 77 K undergoes a negligible shift upon changing the solvent polarity from toluene to a polar glass-freezing alcoholic mixture (4 : 1 = methanol : ethanol) or DMSO (Fig. S9†). Such a behavioral change of the associated S_1 and T_1 states is also reflected in moderate to high spin–orbit coupling values of the two states. Notably, among the three, DPAPCN exhibits the maximum spin–orbit coupling value of 1.32 cm^{-1} between these two states, which may be responsible for its much accelerated RISC rate (Fig. S8†).

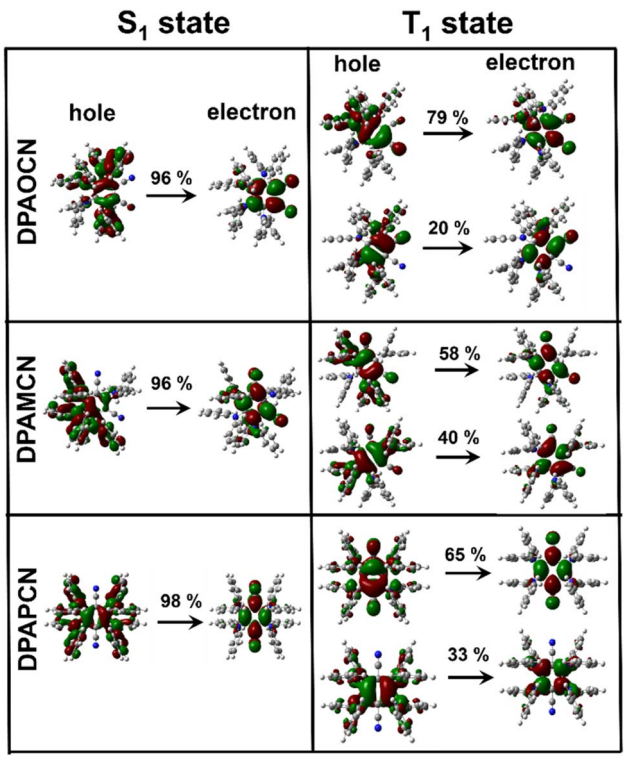

Fig. 3 Natural transition orbital (NTO) analysis for S_1 and T_1 states of all three isomers. Hole and electron pairs of S_1 & T_1 states of DPAOCN, DPAMCN & DPAPCN.

Studying the photo-physical properties of emitter-doped host matrix films is crucial for evaluating their suitability in OLED devices and reducing concentration quenching effects. In our study, we use PMMA as a host matrix due to its high triplet state energy (~3.1 eV), which effectively halts energy transfer from emitters to the host moiety. Time-gated emission spectra of 10 wt% emitter-doped PMMA films align well with the steady-state emission profile, indicating the dominance of the TADF process in all three molecules (Fig. 4a–c). Here also, the delayed fluorescence lifetime is found to be longest in DPAOCN (0.130 ms), followed by DPAMCN (0.104 ms), and shortest in DPAPCN (11.05 μs) (Fig. S10†). Subsequently, DPAPCN has the maximum rate of reverse inter-system crossing (2.9×10^6 s^{-1}) and DPAOCN exhibits the lowest rate (2×10^4 s^{-1}) (Table 1). The variation of k_{RISC} is also consistent with the experimentally measured ΔE_{ST} values, which is found to be the highest in DPAOCN (0.17 eV) and the lowest in DPAPCN (0.06 eV) (Fig. 4d–f). To assess the effect of aggregation on the TADF properties of the isomers, studies on as-prepared pristine powder were carried out. Both DPAMCN and DPAPCN in powder form exhibit an almost complete overlap of steady-state and time-gated emission spectra at different delays indicating a prevailed TADF process (Fig. 5b and c). The TADF lifetimes of DPAMCN and DPAPCN powder in a vacuum are found to be 33 μs and 1.68 μs, respectively. Moreover, temperature-dependent TRPL studies show a gradual decline in delayed emission lifetime with decreasing temperature for both compounds, thus confirming the thermally assisted delayed fluorescence process (Fig. 5e and f). At 77 K, TADF emission intensities of both the luminogens are suppressed, and phosphorescence bands emerged for both DPAMCN and DPAPCN (Fig. S12†). Interestingly, for DPAOCN, the gated emission spectra collected at

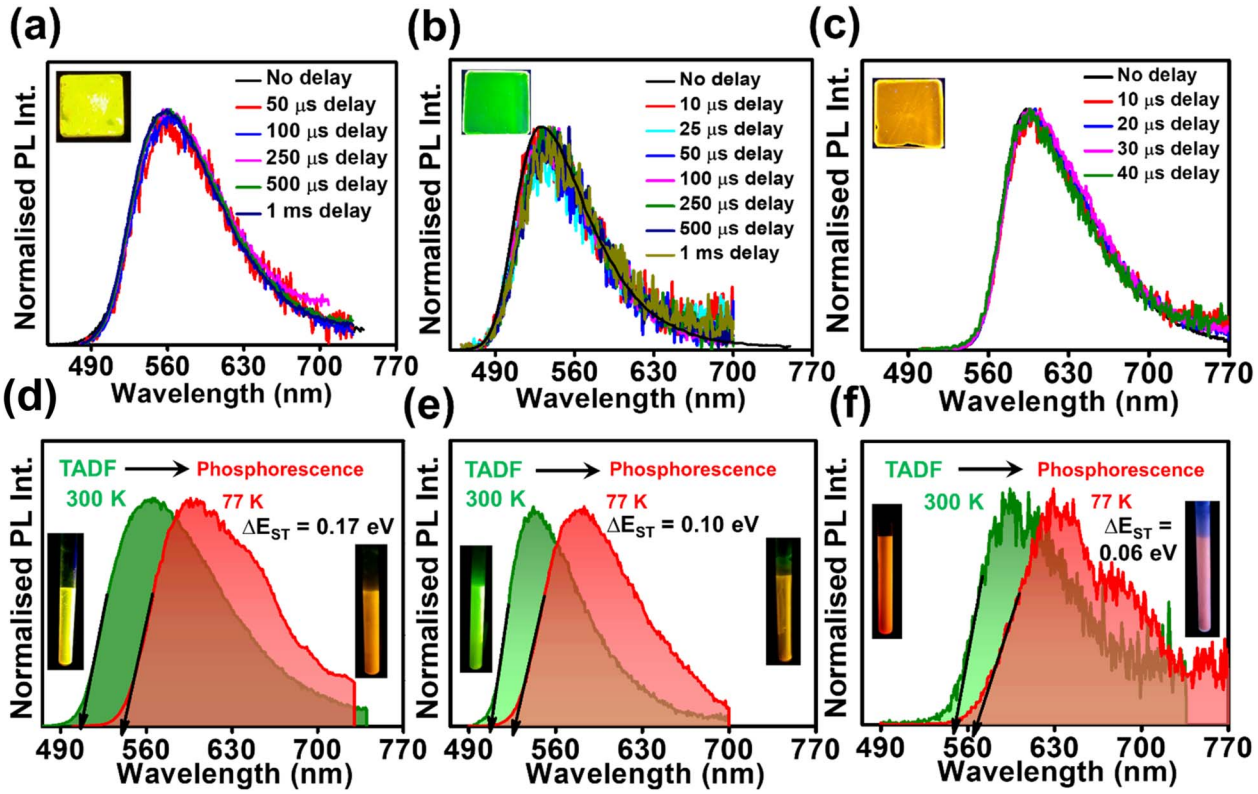

Fig. 4 Time-gated emission spectra of 10 wt% emitter-doped PMMA films of (a) DPAOCN, (b) DPAMCN, and (c) DPAPCN. Time-gated emission spectra of 10 wt% emitter doped PMMA films at RT (298 K) and 77 K for (d) DPAOCN, (e) DPAMCN, and (f) DPAPCN. Time delays for room temperature spectra measurement are kept at 50 μs (for DPAOCN & DPAMCN) and 10 μs (for DPAPCN). For the collection of spectra at 77 K, a 0.25 ms delay has been used for DPAOCN & DPAMCN and a 0.1 ms delay has been used for DPAPCN. Sample windows for all the room temperature spectral measurements have been kept at 2 ms and low-temperature spectral measurements have been kept at 10 ms.

shorter time delays (10 μs and 25 μs) show the dominance of emission from the singlet state (~550 nm) as it matches well with the steady state emission profile, but at a time delay of 50 μs, a red shift in the emission maxima (~600 nm) is observed, accompanied by a small hump at ~550 nm. With further increased time delay, the small hump at ~550 nm disappears and the emission maxima reside at ~600 nm (Fig. 5a). Temperature-dependent lifetime measurements at the two major peaks (550 nm and 600 nm) reveal that the anticipated TADF peak (550 nm) exhibits a decrease in delayed emission lifetime with a decrease in temperature, while the 600 nm peak shows an increased emission lifetime and manifests an ultra-long emission at cryogenic temperatures, indicating phosphorescent emission (Fig. 5d and S13†). The calculated ΔE_{ST} value for DPAOCN is 0.22 eV. Additionally, calculated reverse inter-system crossing (RISC) rates for all three cases reveal the slowest RISC rate (3×10^4 s^{-1}) in DPAOCN, while the most efficient RISC (7.89×10^6 s^{-1}) in DPAPCN, which is consistent with their experimentally obtained ΔE_{ST} values (Table 1). The emergence of room-temperature phosphorescent emission in DPAOCN is likely attributed to the combination of a lower and inefficient RISC rate and a considerably higher SOCME value between T_1 and S_0 states than the other two regio-isomers (1.68 cm^{-1} compared to 0.71 cm^{-1} and 0 of DPAMCN and DPAPCN, respectively) (Fig. S8†). Finally, converted LEDs (c-LEDs) were fabricated from all three isomers for their potential utilization in OLEDs in three different color regimes (see Section B of the application part in the ESI, page no. S56†).

Mechanochromic luminescent (MCL) properties

Crystal symmetry plays a vital role in determining the photophysical properties of luminescent materials. The responsiveness of organic luminogens to external stimuli relies heavily on the presence of a center of inversion in their crystal arrangement.[26,27] Crystals, with a centrosymmetric packing, lack a gross dipole-moment and therefore exhibit degenerate electronic energy states, resulting in no change in emission color under different external stimuli.[26,27] On the other hand, a luminogen with non-centrosymmetric crystal packing can display multi-color emission behavior in response to external stimuli, due to the presence of multiple non-degenerate metastable energy states.[27] In our study, the intriguing aspect that captivates our attention is the crystal packing mode of the regio-isomers. Both DPAMCN and DPAPCN adopt a centrosymmetric $P2_1/C$ space group, whereas DPAOCN crystallizes in a chiral and non-centrosymmetric $P2_12_12_1$ space group (Fig. 6). As previously explained, the presence of a centrosymmetric packing arrangement results in the formation of degenerate energy states when subjected to external stimuli. Consequently, green-

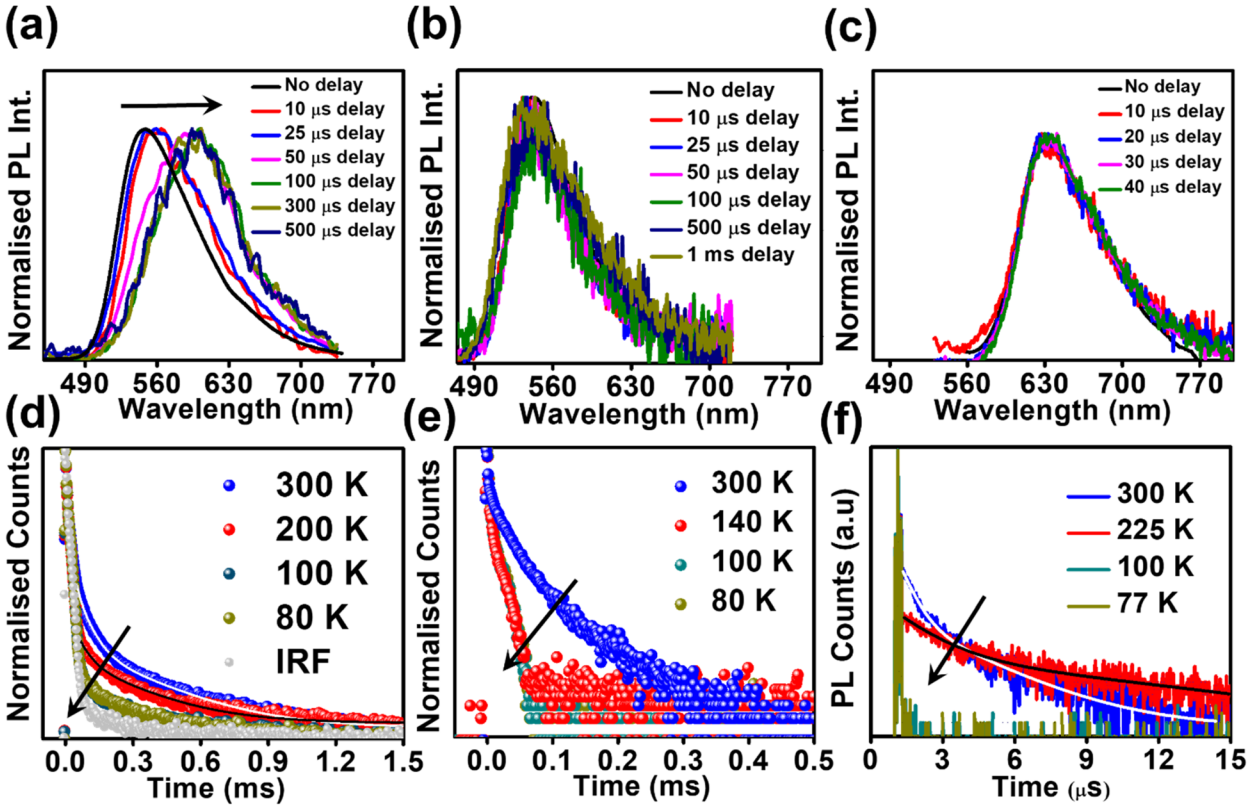

Fig. 5 (a) & (d) Time-gated emission spectra (with varying time delay) and temperature-dependent emission of DPAOCN powder (collected at 550 nm). (b) & (e) Time-gated emission spectra (with varying time delay) and temperature-dependent emission of DPAMCN powder. (c) & (f) Time-gated emission spectra (with varying time delay) and temperature-dependent emission of DPAPCN powder. Sample windows in all cases are kept at 2 ms.

emissive DPAMCN and red-emissive DPAPCN display a minimal shift in their emission profiles upon mechanical grinding with no apparent change in the emission color (Fig. S14†). Intriguingly, DPAOCN in pristine powder form undergoes a ~40 nm red-shift (from ~550 nm to ~590 nm) upon mechanical grinding (with 0.2 gigapascals of pressure) with a visual emission color change from yellow (Y-form, $\Phi = 0.24$) to orange (O-form, $\Phi = 0.10$), thus making DPAOCN a mechanically active luminogen (Fig. 7). At this point, we aimed to determine how mechanical grinding affects the lifetimes of prompt fluorescence (PF) and delayed fluorescence (DF). Regarding *para* and *meta* isomers, there is a minimal alteration in their prompt and delayed fluorescence lifetimes following the grinding process (Fig. S15†). However, a significant change in both prompt and delayed fluorescence lifetimes is observed in the *ortho* isomer (DPAOCN) case. The prompt fluorescence lifetime undergoes a remarkable transformation, increasing from 17 ns in its original state to 5.35 ns after mechanical grinding. Likewise, the delayed fluorescence lifetime experiences a substantial enhancement, transitioning from 353 μs in its pristine state to 473 μs in ground form (Fig. S15†). Such an alternation in emission lifetime is probably due to the large energy difference between the pristine and the ground form[28] (see Note 1, page S50 in the ESI†). The reversible switching ability from the ground state to the initial pristine state is crucial for the reusability of mechanochromic materials. Interestingly, exposure to DCM vapor causes the compound to revert back to its original color (Fig. 7c), resembling the pristine state (Y-form). However, extended exposure of the ground powder to DCM vapor or heating the ground sample at around 90 °C results in the emergence of a different state exhibiting green emission ('G-form', emission maxima at 539 nm, $\Phi = 0.09$) (Fig. 7 and S16†) (see Note 2 in the ESI, page S51†). Thus, DPAOCN with non-centrosymmetric packing mode exhibits tri-color mechanochromic luminescence along with simultaneous TADF and RTP. The simultaneous manifestation of these properties in a single compound is exceedingly rare in the literature. It is noteworthy to mention that exposing the green emissive DCM-soaked powder to air overnight and subsequently grinding it again using a mortar and pestle results in the formation of the Y-form and O-form, respectively (Fig. 7c). This demonstrates the reversibility of all the steps involved in the process. In addition to the symmetry factor, another deciding factor that can dictate the mechanochromic properties of a certain molecule is the amount of void space in the crystal unit cell.[29] The amount of void present in a crystal is a combined effect of short-contact non-covalent interactions and the degree of flexibility of the molecular arrangement. In order to quantitatively evaluate each type of non-covalent interaction, Hirshfeld surface analysis is performed and the contribution of each type of non-covalent

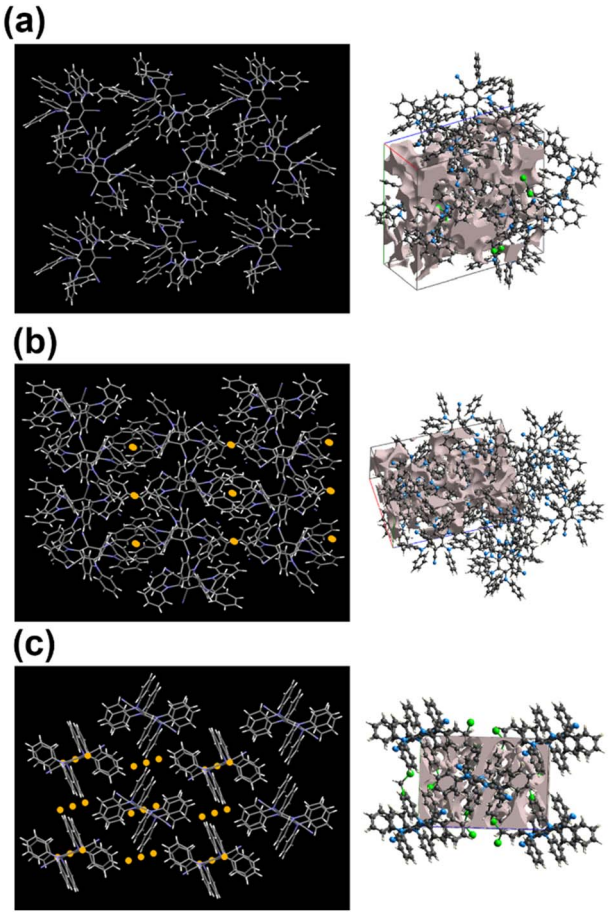

Fig. 6 (a) Non-centrosymmetric crystal packing and crystal voids inside a unit cell of DPAOCN. (b) Centrosymmetric crystal packing along with the center of inversion (i) symmetry elements (shown as yellow dots) and crystal voids inside a unit cell of DPAMCN. (c) Centrosymmetric crystal packing along with the center of inversion (i) symmetry elements (shown as yellow dots) and crystal voids inside a unit cell of DPAPCN.

interaction is highlighted in Fig. S17–S19.† Looking into the void space volume of each crystal, the maximum void space is obtained for DPAOCN (826 Å^3), then comes DPAMCN (597 Å^3), and the minimum is obtained for DPAPCN (with only 280 Å^3 of void volume) (Fig. 6). The higher void space in DPAOCN is probably due to its more sterically hindered molecular architecture which restricts the neighbouring molecules from approaching closer to each other, creating a higher void volume in the unit cell (Fig. 6 and S20†). Notably, the steric hindrance follows the trend DPAOCN > DPAMCN > DPAPCN as does the void volume. The maximum void volume in DPAOCN can provide more flexibility in the molecular scaffold and thus, upon external stimuli, twisted terminal diphenyl moieties ($O_1 = 58^\circ$, $O_2 = 63^\circ$, $O_3 = 55^\circ$, and $O_4 = 63^\circ$) of DPAOCN can alter the dihedral angle with the acceptor core (Fig. S21†), modulating the extent of charge transfer and thereby changing its emission energy, color and lifetime. PXRD analysis is further carried out to look into the details of the possible phase transition of the isomers upon mechanical treatment. The simulated PXRD

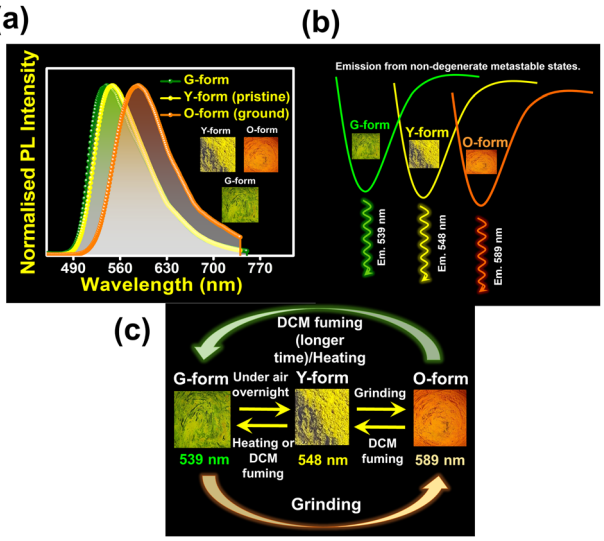

Fig. 7 (a) DPAOCN pristine powder undergoing a red shift upon mechanical grinding (ex. 370 nm). (b & c) scheme of tri-color emission & multi-stimuli responsive behavior of DPAOCN under several external stimuli (photos collected using a 365 nm UV lamp).

pattern of all the isomers aligns well with the experimentally obtained PXRD patterns (Fig. S22–S23†). All the luminogens exhibit sharp and highly intense diffraction peaks in pristine powder form suggesting a high degree of crystallinity in the samples. Upon grinding, intensities of some sharp diffraction peaks decreased with the appearance of broad and diffused PXRD patterns, suggesting an increase in the amorphous nature of the samples in the ground state. Although such modulation of crystallinity in DPAMCN and DPAPCN does not lead to an energetically different phase, but just enough to exhibit MCL properties, in DPAOCN however, it leads to an orange emissive 'O-form', energetically much different from the pristine yellow emissive original 'Y-form'. Most importantly, upon DCM vapor treatment (with nearly 2% of DCM concentration, discussed in Note 2 of the ESI†), the reversibility to the original pristine state is confirmed by the reappearance of sharp and intense diffraction peaks along with the broad halo disappearing from the PXRD pattern (Fig. S22†). Finally, the reversible tri-color emission characteristics of DPAOCN have been further utilized in rewritable media applications (details in Section D of the application part in the ESI, page no S60†).

SHG properties

Organic non-linear optical (NLO) materials have emerged as promising alternatives to inorganic NLO systems due to their high hyperpolarizabilities, diverse topologies, ease of processing, and high stability.[30,31] Notably, the absence of inversion symmetry is the key prerequisite for a material to exhibit any second-order nonlinear process.[32,33] Nonetheless, DPAOCN stands out as the best candidate to exhibit second harmonic generation properties among the three molecules, as it exhibits non-centrosymmetric crystal packing with the $P2_12_12_1$ space group. Our research involved performing extensive

measurements on our sample using second harmonic generation (SHG) in a range of wavelengths along with second-order non-linear susceptibility ($\chi^{(2)}$) and optical stability. To conduct these experiments, we have used ultrafast pulses generated from an optical parametric amplifier (OPA) with a pulse width of approximately 50 fs.[34,35] Details of the experimental setup and procedure can be found in Section A of the ESI.† Non-centrosymmetric DPAOCN exhibits a significantly strong SHG response upon excitation in the 1160 – 1340 nm wavelength range. Fig. 8a shows the SHG response obtained from DPAOCN at a constant power of 2.5 mW, whereas Fig. 8b plots the SHG intensity *vs.* SHG wavelength. It is evident that the maximum SHG is obtained at 610 nm, which corresponds to an excitation with 1220 nm light. Notably, the maximum signal is at the absorbance band-edge of DPAOCN crystals owing to an enhanced light–matter interaction,[36] also known as the band-edge resonance effect (Fig. SA3 of Section A in the ESI, page S55†). We have also observed a weak THG response of our sample within the same excitation wavelength (Section A-Fig. SA2 of the ESI†). To determine $\chi^{(2)}$ of DPAOCN, we have exploited Maxwell's equation of relative intensity (Section A-Fig. SA1 of the ESI†). Here potassium dihydrogen phosphate (KDP) is used as the reference SHG material to calculate the second-order susceptibility. KDP has a $\chi^{(2)}$ value of 0.37 pm V^{-1} at 1064 nm.[37–41] The $\chi^{(2)}$ value of the DPAOCN is obtained to be around 0.19 pm V^{-1} at 1220 nm (SHG output 610 nm) at which wavelength DPAOCN shows the maximum SHG. The above results suggest that DPAOCN has a much stronger SHG response at 610 nm compared to even KDP. When considering a material for use as a potential source for nonlinear optics, it is essential to take into account both its NLO efficiency and optical stability. To assess the latter, we determined the laser-induced damage threshold (LIDT) of DPAOCN. The LIDT is the excitation power level at which the SHG response deviates from the expected quadratic dependence on excitation power. To find the LIDT, we measured the SHG intensity at varying excitation power levels, specifically at an excitation wavelength of 1220 nm, which corresponds to the maximum SHG response of DPAOCN. Fig. 7c and d display the relationship between excitation power and SHG intensity, along with its quadratic fit. It becomes evident that the quadratic nature of the power dependence is lost at around 3 mW, due to saturation effects such as local heating. We found the LIDT value of DPAOCN to be 13.27 GW cm^{-2} (detailed calculation shown in Section A of the ESI†), which is comparable to those of other popular commercially available SHG materials such as BBO (~10 GW cm^{-2}) and KDP (~3 GW cm^{-2}). Therefore, DPAOCN proves to be both highly efficient in terms of second-order susceptibility and optically stable, making it a suitable material for practical SHG applications.

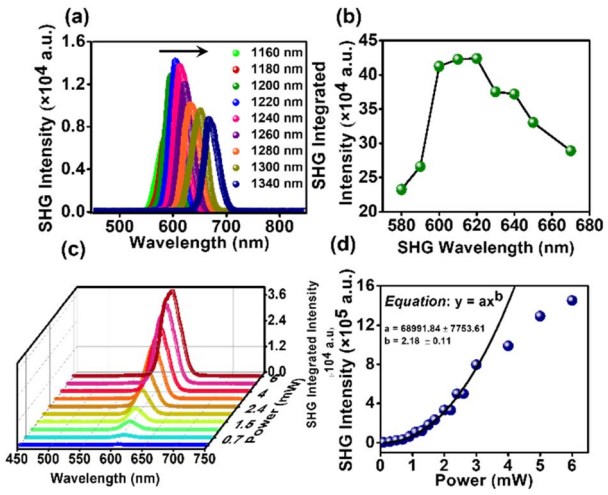

Fig. 8 (a) Wavelength-dependence of the SHG responses in the 1160–1340 nm region, (b) dependence of SHG integrated intensities with varying SHG wavelengths for DPAOCN crystals, (c) power-dependent study of the SHG responses at 610 nm for DPAOCN crystals, and (d) quadratic fit of the SHG intensities with varying excitation power.

Applications

Two-photon cell imaging. Due to their greater optical penetration, excellent spatial resolution, and minimal optical scattering, two-photon-excited organic luminogens have attracted significant attention in comparison to typical one-photon-excited fluorophores.[42–45] Such "two-photon absorption" active materials are particularly useful for cell imaging since they

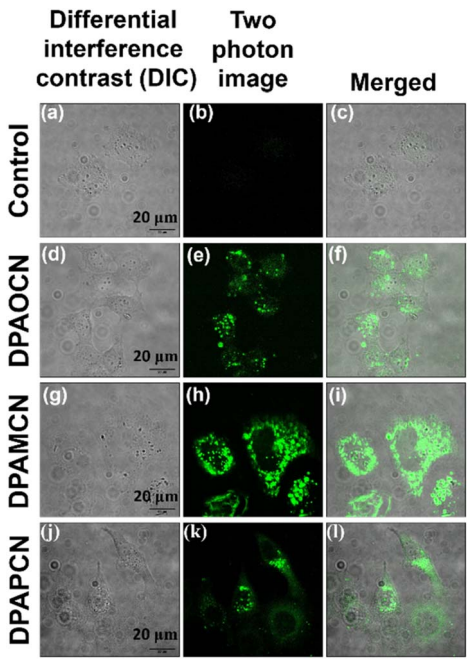

Fig. 9 Two-photon microscopy image (excitation wavelength = 800 nm and collection window is from 530 nm to 620 nm for DPAOCN, 510 nm to 580 nm for DPAMCN, and 550 to 630 for DPAPCN) of MCF-7 cells: top row-without dye treatment or the control and the rests-with10 μM dye treatment. (a, d, g and j) Differential interference contrast (DIC) images, (b) cells without dye treatment, the two-photon image of cells treated with dye (e) DPAOCN, (h) DPAMCN and (k) DPAPCN and (c, f, i and l) DIC image merged with dye treated confocal images.

inflict the target cell with the least amount of photo damage. Large π-conjugated organic chromophores with enforced co-planarity and donor–acceptor groups at the center or at the end of the molecular scaffolds tend to exhibit strong two–photon absorption behavior[46] due to higher transition dipole moment values between the ground, intermediate, and final states. Our molecules' strong charge transfer behavior prompted us to investigate their two-photon absorption behavior and here, it is discovered that all three luminogens are two-photon active in both the liquid and solid crystalline states (Fig. SC1 & SC2, Section C† of the application part). We conduct a two-photon cell imaging experiment as a result of these exciting features. It is clear from the two-photon image that our luminogens can effectively illuminate cells, mainly the cytoplasmic part (Fig. 9). Additionally, the MTT viability assay of MCF7 cells is used to investigate the cytotoxic behavior of our luminogens with no significant cell death (more than 50%) up to 15 μM (Fig. SC3 of Section C in the ESI†) of the dye concentration.

Conclusions

Overall, the trifecta of TADF, SHG, and mechanochromic luminescence (MCL) among three donor–acceptor based regio-isomers has been successfully studied in this research article. Through extensive experimentation, we have established that TADF properties can be thoroughly tuned from the *ortho* to the *para* isomer. Herein, the *ortho*-isomer, DPAOCN, exhibits the slowest rate of reverse intersystem crossing (RISC) ($\sim 10^2$–10^4 s^{-1}), whereas the *para*-isomer, DPAPCN, dazzles with the highest TADF efficiency with an RISC rate of near $\sim 10^6$ s^{-1}. These differences in TADF efficiency mainly stem from the variation in energy splitting (ΔE_{ST}) values and the extent of spin–orbit coupling (SOC) between the lowest singlet and triplet states. Moreover, the crystal space groups of all three isomers are different, as the *ortho*-isomer adopts a non-centrosymmetric and chiral $P2_12_12_1$ space group, whilst the other two crystallize in the centrosymmetric $P2_1/C$ space group. Intriguingly, the non-centrosymmetric crystal packing of the *ortho*-isomer opened up two different avenues of photonics research. It exhibits excellent mechanochromic luminescence behavior with green, yellow, and orange emissions along with outstanding SHG characteristics with a $\chi^{(2)}$ value of 0.19 pm V^{-1} at 1220 nm and LIDT value of 13.27 GW cm^{-2}. To the best of our knowledge, it is the first ever reported organic luminogen to exhibit simultaneous TADF, SHG, and mechanochromic luminescence properties. Furthermore, the electroluminescence potential of all three isomers has been explored by converted LED (cLED) device fabrication. Also, the isomers have demonstrated two-photon absorption activity in both solution and crystal states. This unique characteristic has been successfully exploited in two-photon confocal cell imaging, without significant cell death observed at concentrations up to 15 μM of the dye.

Data availability

Data supporting this study is available within the ESI† and from the authors on reasonable request.

Author contributions

AC and PH came up with the idea for the project. AC is the primary contributor in terms of design and development, execution, and compilation of the project. The electronic structure calculations were performed by AC and SS. The interpretation of the theoretical results is the combined effort of AC and SS. AC and JC worked together to carry out fluorescence up-conversion measurements. JC played a key role in improving the writing part and figures for the manuscript. HA contributed to conducting low-temperature TRPL studies. Under the guidance of PM, RT conducted the second harmonic generation experiment. RMU performed the two-photon cell imaging experiment, and ML supervised the two-photon cell imaging experiment. MDA helped in solving the crystal structures. PH supervised the whole project and provided valuable insights throughout the progression of the project.

Conflicts of interest

There are no conflicts to declare.

Acknowledgements

PH and PM acknowledge the Science and Engineering Research Board (DST-SERB), Government of India for financial support through grant numbers CRG/2020/000567 and CRG/2020/002699, respectively. The support and the resources provided by the 'PARAM Brahma Facility' under the National Supercomputing Mission, Government of India at IISER Pune are gratefully acknowledged. AC and JC are thankful to IISER Pune for its excellent facilities and fellowships. RT & HA thank UGC, India for a fellowship. The authors thank Dr Rangarajan Bakthavatsalam and his supervisor, Dr Janardan Kundu from IISER Tirupati, for their valuable assistance in the low-temperature TRPL measurement of a sample. The authors acknowledge the IISER Pune microscopy facility and Mr Vijay Vittal for two-photon imaging experiments. Ms. Anindita Bhowmick from the Prof. RGB group, IISER Pune is acknowledged for her valuable suggestions during the synthesis of the designed luminogens. SS thanks the Gdansk University of Technology for the Nobelium grant (No. 16/2021/IDUB/I.1) under "The Excellence Initiative – Research University" (IDUB) programme. The authors would like to acknowledge Dr Palash Banerjee from NCL Pune for his help in TGA data measurements.

References

1 S. Qi, S. Kim, V.-N. Nguyen, Y. Kim, G. Niu, G. Kim, S.-J. Kim, S. Park and J. Yoon, *ACS Appl. Mater. Interfaces*, 2020, **12**, 51293–51301.
2 Y. Tao, K. Yuan, T. Chen, P. Xu, H. Li, R. Chen, C. Zheng, L. Zhang and W. Huang, *Adv. Mater.*, 2014, **26**, 7931–7958.
3 G. Hong, X. Gan, C. Leonhardt, Z. Zhang, J. Seibert, J. M. Busch and S. Bräse, *Adv. Mater.*, 2021, **33**, 2005630.
4 M. Y. Wong and E. Zysman-Colman, *Adv. Mater.*, 2017, **29**, 1605444.

5 F. Fang, L. Zhu, M. Li, Y. Song, M. Sun, D. Zhao and J. Zhang, *Adv. Sci.*, 2021, **8**, 2102970.
6 M. A. Bryden and E. Zysman-Colman, *Chem. Soc. Rev.*, 2021, **50**, 7587–7680.
7 G. Li, F. Zhan, W. Lou, D. Wang, C. Deng, L. Cao, Y. Yang, Q. Zhang and Y. She, *J. Mater. Chem. C*, 2020, **8**, 17464–17473.
8 H. Uoyama, K. Goushi, K. Shizu, H. Nomura and C. Adachi, *Nature*, 2012, **492**, 234–238.
9 Z. Xie, C. Cao, Y. Zou, X. Cao, C. Zhou, J. He, C. S. Lee and C. Yang, *Adv. Funct. Mater.*, 2022, **32**, 2112881.
10 W. Li, B. Li, X. Cai, L. Gan, Z. Xu, W. Li, K. Liu, D. Chen and S. J. Su, *Angew. Chem., Int. Ed.*, 2019, **58**, 11301–11305.
11 D. G. Congrave, B. H. Drummond, P. J. Conaghan, H. Francis, S. T. E. Jones, C. P. Grey, N. C. Greenham, D. Credgington and H. Bronstein, *J. Am. Chem. Soc.*, 2019, **141**, 18390–18394.
12 T. Hatakeyama, K. Shiren, K. Nakajima, S. Nomura, S. Nakatsuka, K. Kinoshita, J. Ni, Y. Ono and T. Ikuta, *Adv. Mater.*, 2016, **28**, 2777–2781.
13 J.-X. Chen, W.-W. Tao, W.-C. Chen, Y.-F. Xiao, K. Wang, C. Cao, J. Yu, S. Li, F.-X. Geng, C. Adachi, C.-S. Lee and X.-H. Zhang, *Angew. Chem., Int. Ed.*, 2019, **58**, 14660–14665.
14 Y. Song, M. Tian, R. Yu and L. He, *ACS Appl. Mater. Interfaces*, 2021, **13**, 60269–60278.
15 M. Yu, X. Zhu, J. Zeng, H. Liu, R. Huang, Z. Zhuang, P. Shen, Z. Zhao and B. Z. Tang, *J. Mater. Chem. C*, 2021, **9**, 14808–14814.
16 H. F. Higginbotham, C.-L. Yi, A. P. Monkman and K.-T. Wong, *J. Phys. Chem. C*, 2018, **122**, 7627–7634.
17 D. Lei, J.-H. Song, Z.-L. Wu, J.-X. Hu, Y.-S. Wang, D.-H. Zhang, L. Meng, X.-L. Chen and C.-Z. Lu, *J. Mater. Chem. C*, 2023, **11**, 8626–8633.
18 Y. Liu, J. Yang, Z. Mao, Y. Wang, J. Zhao, S. J. Su and Z. Chi, *Chem. Sci.*, 2023, **14**, 1551–1556.
19 S. K. Pathak, G. Li, C. Zhou, Z. Wang and H. Liu, *J. Mater. Chem. C*, 2023, **11**, 6685–6694.
20 R. Ishimatsu, S. Matsunami, T. Kasahara, J. Mizuno, T. Edura, C. Adachi, K. Nakano and T. Imato, *Angew. Chem., Int. Ed.*, 2014, **53**, 6993–6996.
21 R. Ishimatsu, S. Matsunami, K. Shizu, C. Adachi, K. Nakano and T. Imato, *J. Phys. Chem. A*, 2013, **117**, 5607–5612.
22 K. K. Jha, S. Dutta and P. Munshi, *Cryst. Growth Des.*, 2018, **18**, 1126–1135.
23 M. Jin, T. Seki and H. Ito, *J. Am. Chem. Soc.*, 2017, **139**, 7452–7455.
24 S. Guerin, S. A. M. Tofail and D. Thompson, *NPG Asia Mater.*, 2019, **11**, 1–5.
25 T. Moitra, P. Karak, S. Chakraborty, K. Ruud and S. Chakrabarti, *Phys. Chem. Chem. Phys.*, 2021, **23**, 59–81.
26 B. Roy, M. C. Reddy, S. N. Panja and P. Hazra, *J. Phys. Chem. C*, 2019, **123**, 3848–3854.
27 B. Xu, W. Li, J. He, S. Wu, Q. Zhu, Z. Yang, Y.-C. Wu, Y. Zhang, C. Jin, P.-Y. Lu, Z. Chi, S. Liu, J. Xu and M. R. Bryce, *Chem. Sci.*, 2016, **7**, 5307–5312.
28 M. Yang, I. S. Park, Y. Miyashita, K. Tanaka and T. Yasuda, *Angew. Chem., Int. Ed.*, 2020, **59**, 13955–13961.
29 B. Roy, M. C. Reddy and P. Hazra, *Chem. Sci.*, 2018, **9**, 3592–3606.
30 S. Semin, X. Li, Y. Duan and T. Rasing, *Adv. Opt. Mater.*, 2021, **9**, 2100327.
31 A. Miniewicz, S. Bartkiewicz, E. Wojaczynska, T. Galica, R. Zalesny and R. Jakubas, *J. Mater. Chem. C*, 2019, **7**, 1255–1262.
32 A. Dey and G. R. Desiraju, *Chem. Commun.*, 2005, 2486–2488.
33 R. W. Boyd, H. Shin, M. Malik, C. O'Sullivan, K. W. C. Chan, H. J. Chang, D. J. Gauthier, A. Jha, J. Leach, S. Murugkar and B. Rodenburg, in *Nonlinear Optics*, Optica Publishing Group, Kauai, Hawaii, 2011, p. NWC2.
34 S. Maqbool, Z. Thekkayil and P. Mandal, *Adv. Opt. Mater.*, 2023, 2202942.
35 R. Chakraborty, P. K. Rajput, G. M. Anilkumar, S. Maqbool, R. Das, A. Rahman, P. Mandal and A. Nag, *J. Am. Chem. Soc.*, 2023, **145**, 1378–1388.
36 P. P. Markowicz, H. Tiryaki, H. Pudavar, P. N. Prasad, N. N. Lepeshkin and R. W. Boyd, *Phys. Rev. Lett.*, 2004, **92**, 83903.
37 N. Youngblood, R. Peng, A. Nemilentsau, T. Low and M. Li, *ACS Photonics*, 2017, **4**, 8–14.
38 L. Yao, Z. Zeng, C. Cai, P. Xu, H. Gu, L. Gao, J. Han, X. Zhang, X. Wang, X. Wang, A. Pan, J. Wang, W. Liang, S. Liu, C. Chen and J. Tang, *J. Am. Chem. Soc.*, 2021, **143**, 16095–16104.
39 Y. Xie, F. Liang, B. Zhang, B. Ge, H. Yu, Z. Lin, Z. Wang, H. Zhang, B. Huang and J. Wang, *ACS Omega*, 2019, **4**, 1045–1052.
40 F. O. Saouma, C. C. Stoumpos, J. Wong, M. G. Kanatzidis and J. I. Jang, *Nat. Commun.*, 2017, **8**, 742.
41 R. C. Eckardt, H. Masuda, Y. X. Fan and R. L. Byer, *IEEE J. Quantum Electron.*, 1990, **26**, 922–933.
42 T. Liu, L. Xu, H. Wang, B. Chen and S. Shi, *ACS Appl. Bio Mater.*, 2023, **6**(7), 2849–2859.
43 Q. Lu, C.-J. Wu, Z. Liu, G. Niu and X. Yu, *Front. Chem.*, 2020, **8**, 1205.
44 L. Xu, J. Zhang, L. Yin, X. Long, W. Zhang and Q. Zhang, *J. Mater. Chem. C*, 2020, **8**, 6342–6349.
45 Y. Wang, H. Wu, P. Li, S. Chen, L. O. Jones, M. A. Mosquera, L. Zhang, K. Cai, H. Chen, X.-Y. Chen, C. L. Stern, M. R. Wasielewski, M. A. Ratner, G. C. Schatz and J. F. Stoddart, *Nat. Commun.*, 2020, **11**, 4633.
46 A. Chatterjee, J. Chatterjee, S. Sappati, T. Sheikh, R. M. Umesh, M. D. Ambhore, M. Lahiri and P. Hazra, *J. Phys. Chem. B*, 2021, **125**, 12832–12846.